Supporting Online Material

Local Relative Density Modulates Failure and Strength in Vertically Aligned Carbon Nanotubes

Siddhartha Pathak [1*], Nisha Mohan [1], Elizabeth Decolvenaere [1], Alan Needleman [2], Mostafa Bedewy [3], A. John Hart [3], Julia R. Greer [1]

[1] Materials Science, California Institute of Technology (Caltech), Pasadena, CA, USA
[2] Department of Materials Science and Engineering, College of Engineering and Center for Advanced Scientific Computing and Modeling (CASCaM), University of North Texas, Denton, TX, USA.
[3] Mechanosynthesis Group, Department of Mechanical Engineering, University of Michigan, Ann Arbor, MI, USA.

[*] Contact author (Present address): MPA-CINT Center for Integrated Nanotechnologies, Los Alamos National Laboratory, P. O. Box 1663, MS - K771, Los Alamos , NM, 87545, Phone: +1 (505) 667-2082, Fax: +1 (505) 665-9030, E-mail: pathak@caltech.edu, siddharthapathak@gmail.com

1. Compressive Behavior of Vertically Aligned Carbon Nanotube (VACNT) forests: from literature

The method by which VACNTs are synthesized is the primary factor affecting their complex, hierarchical morphology. This microstructure, in turn, affects their mechanical behavior, in particular the modulus, buckling strength, and recoverability. Synthesis techniques for VACNTs can be divided into two main categories: the chemical vapor deposition (CVD) synthesis method where the VACNT film is coated onto an existing substrate, and the carbide-derived carbon (CDC) synthesis method, [1] where carbon is formed by selective extraction of the metal or metalloid atoms in the carbide (*e.g.*, silicon carbide), transforming the carbide structure into pure carbon. Even within materials grown via CVD, control of the growth conditions, such as the atmosphere, catalyst activity, and pressure, are known to significantly affect the repeatability of the VACNT's morphology and hence the consistency of mechanical properties. [2] For example, using 'floating' *vs.* 'fixed' catalysts [3] in the CVD syntheses [4] have been shown to result in vastly different VACNT morphologies.

Figure S1 highlights four literature examples of the differences in the mechanical response of various CVD-VACNT micro-pillars subjected to compression. Note in particular the higher stiffness and strength of the VACNTs grown using the floating catalyst technique in Fig S1a, [5] as compared to the ones grown using the fixed catalyst method (Figs. S1b, [3] S1c [6] and S1d [7]). Other differences between these nominally identical VACNT samples are the ability of some of them to recover almost completely after large compressions (Figs. S1a and c) while others deform permanently even at modest strains [7-11] (Figs. S1b and d).

Figure S1 also demonstrates the similarities in the deformation characteristics of the various VACNT systems. All of the four VACNT systems show 3 distinct regimes in their stress-strain response – elastic, plateau and densification – similar to open-cell foams. Unlike foams however, the plateau region in the VACNTs generally has a positive slope, which can vary significantly between VACNT samples. The slopes of the plateau region were calculated to be 11, 5 and 0.6 MPa for Figs. S1a, c and d, respectively. Note also that all VACNT systems shown in Fig. S1a exhibit a bottom-to-top sequence of buckling. Here the first buckle generally nucleates close to the substrate, and each subsequent lateral collapse event initiates only after the preceding one was completed, thus sequentially collapsing the entire structure. [3, 5-7] We are unaware of any literature report that suggests a different buckling sequence (such as top-to-bottom or otherwise) for VACNT pillars under compression.

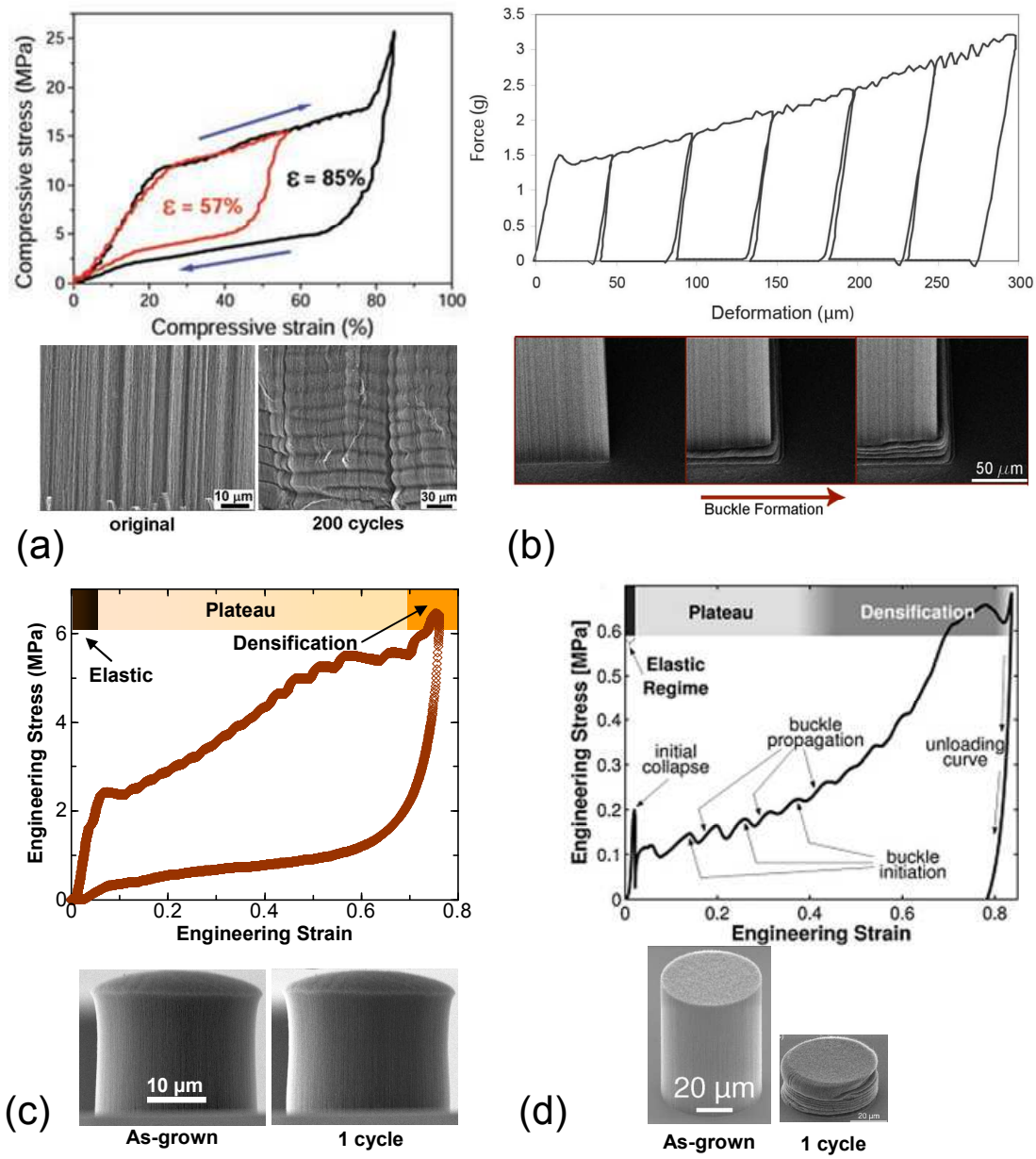

Figure S1. VACNT behavior under compression for (a) 860 μm thick VACNT array, [5] (b) 400 μm diameter CNT column [3] (c) 30 μm × 30 μm (diameter × height) VACNT micro-pillar [6] and (d) 50 μm × 60 μm (diameter × height) VACNT micro-pillar. [7] All of these VACNT systems show 3 distinct regimes in their stress-strain response – elastic, plateau and densification – similar to open-cell foams. Unlike foams, the plateau region in the VACNTs generally has a strong positive slope. All VACNT systems also exhibit a bottom-first sequence of buckling.

These VACNT systems differ widely in their ability to recover from large deformations. Thus while both VACNT systems in (a) and (c) show an almost complete recovery, even after multiple cycles, the VACNT systems in (b) and (d) do not exhibit any appreciable recovery, even at modest strain levels.

2. Image Analysis Procedure

Figure S2 shows the details of the protocol followed for the image analysis on the VACNT micro-pillars. During imaging, the samples were tilted to 30° with respect to the direction of the electron beam and 9-10 images at evenly spaced intervals were taken along the height of each pillar, as shown in Fig S2a. The imaging conditions were fixed at 100 kX magnification, 10 kV accelerating voltage, at a working distance of 6 mm. This allowed a large enough representative area of the VACNT forest to be imaged while maintaining an adequate resolution of the individual CNTs and bundles. Further attention is needed during image-capture since subsequent analysis of the images by the Canny algorithm [12] requires that the intensity spectrum of the images be captured in its entirety. This was achieved by maintaining a constant contrast value for all of the images along the sample height. Only the brightness was adjusted (if needed) in order to ensure that the intensity spectrum was not clipped off.

To avoid any loss in resolution due to the 30° tilt of the samples, only the central 10% of each image was used for image analysis, as demonstrated in Figs. S2c and e. Each image was first converted to grayscale (Figs. S2b and c), and then analyzed using edge detection technique (described in detail in Eq. 2).

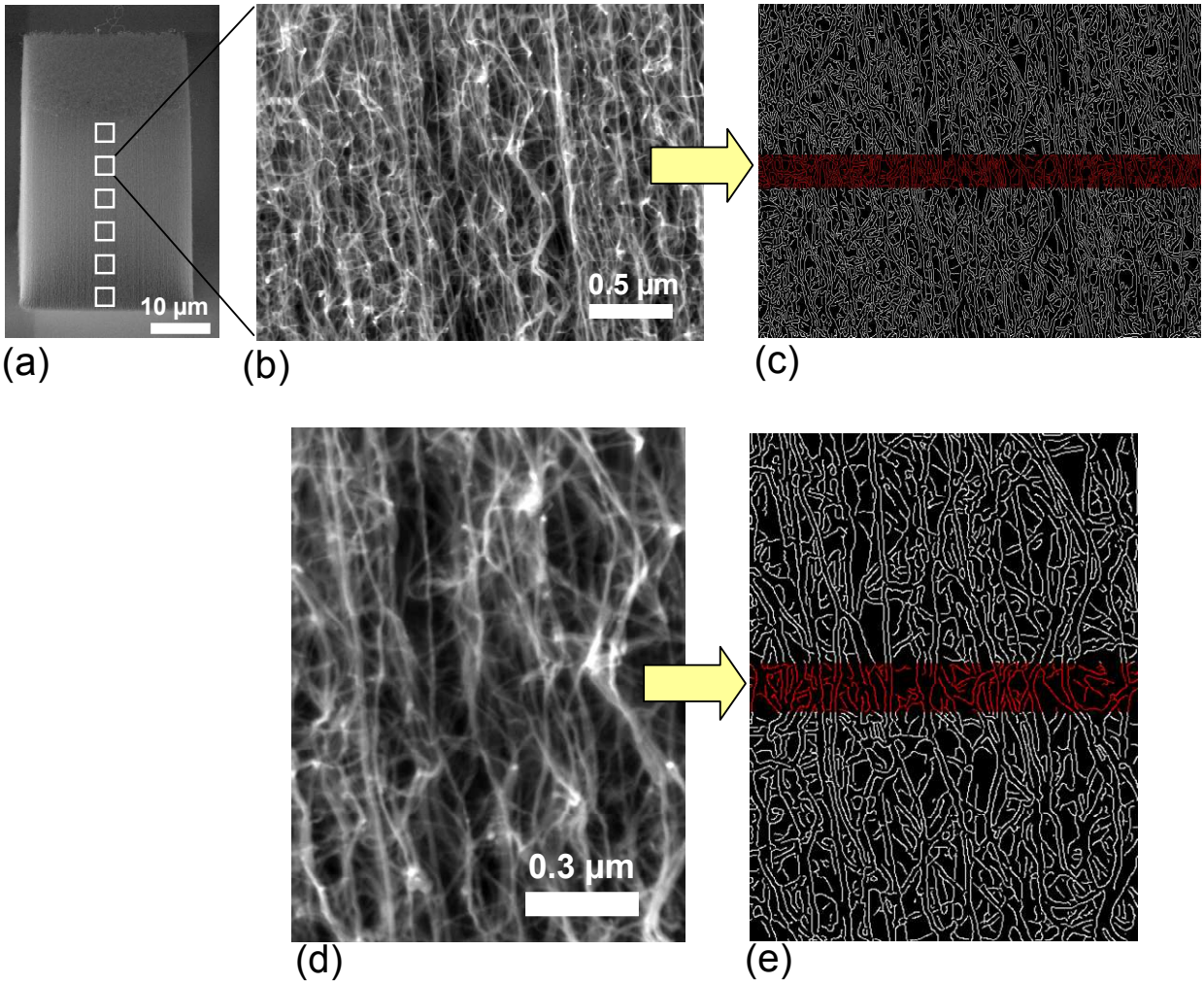

Figure S2. (a) For image analysis 9-10 images at evenly spaced intervals were taken along the height of each pillar. To compute the CNT number density, each captured image (b) was converted to grayscale, and the edges were isolated using the Canny algorithm [12] (c). A magnified version is shown in (d) and (e).

To avoid any loss in resolution due to the 30° tilt of the samples, only the central 10% of each image was used for image analysis, as demonstrated by the red strips in (c) and (e).

The SEM images were taken at a 30 deg tilt angle.

3. Verification of the Image Analysis Protocol

The efficacy of ζ (Eq. 2) as a reliable figure of merit for representing the CNT number density was verified by crosschecking the values obtained from Eq. 2 with manual counting procedures. For this purpose, a series of additional SEM images of the same samples were taken at a higher magnification of 200 kX and analyzed via the method described in Fig. S2 using a pixel radius of 6. These same images were overlaid with five horizontal lines, and the crossings between these lines and tubes in the images were manually counted. Some examples of this comparison are shown below in Fig. S3.

While there are some differences in the values calculated from the manual counting technique *vs.* the edge detection algorithm, the trends and the peaks/valleys in the data seem to match pretty well between the two techniques, as shown in Figs. S3a and b. This suggests that the Canny method may represent an accurate approach to determine the relative local tube number density variation within the same sample.

The repeatability of our image analysis techniques is also a concern, since a slight change in the session-to-session SEM imaging conditions can potentially cause a large variation in ζ. Moreover the edge-detection algorithm works only at a high enough magnification where individual CNTs can be resolved. Thus a site-to-site variation in the ζ values is also a possibility if a very high magnification is used. In order to assuage both these concerns a multi-day imaging protocol was followed, where the same pillar was imaged over different SEM sessions (over multiple days). As shown in Fig. S4, images taken over multiple days displayed the same trends. It is interesting to note that while the absolute numbers do vary somewhat between the two data-sets (as is expected), both datasets show the same sudden drop at around a pillar height of 25 μm. Note that these variations in the absolute number counts are accounted for in the normalization protocol defined for ζ (Eq. 2). Moreover in this work the reported data (shown in Fig. 2 of the paper) has been averaged over 3 pillar sets for each case. This averaging is expected to mitigate any minor fluctuations in the individual datasets. Data was obtained from over 60 images on 6 pillars in this work via the image analysis technique described above, and the consistent nature of these values strongly suggests that the observed trends are real.

The image analysis technique was also applied across the width of the VACNT pillars. As shown in Fig. S5, the absolute tube number counts are more or less constant – they range within 80-85 counts – across the width of the imaged square pillar. This ensures that there are no significant variations in the values of ζ in the lateral direction.

Figure S6 shows a representative sample of SEM images taken along the heights of the pillars on the substrate-edge (Fig. S6a) and of pillars in the interior of the substrate (Fig. S6b). A representative set of 4 images are shown for each set. These images were analyzed using Eq. (2) in order to calculate their respective ζ values. Note that a visual inspection of the SEM images in this figure might indicate some differences in their tortuosity (in addition to their number densities); however tortuosity differences are not accounted for in Eq. (2).

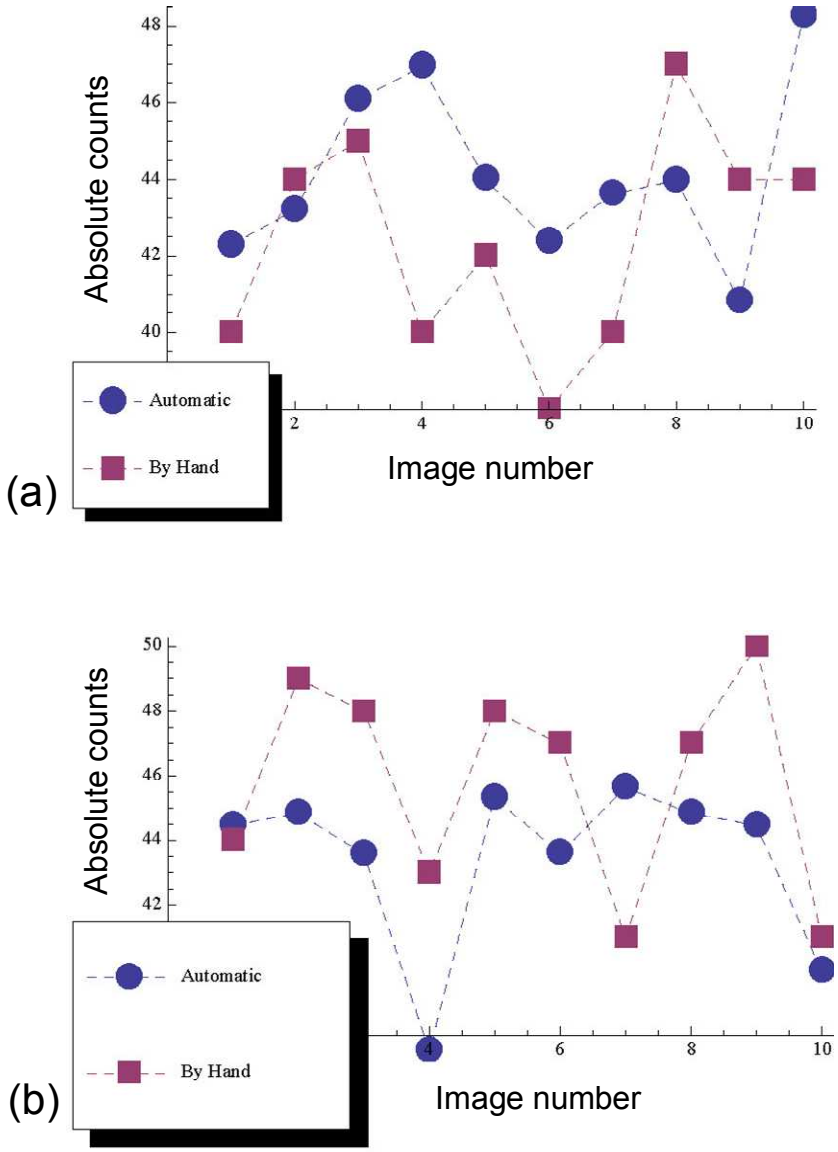

Figure S3. Crosschecking the values obtained using the edge detection technique (Eq. 2) vs. manual counting procedures for (a) pillars on the substrate interior and (b) pillars on substrate edge. The x-axis denotes the image numbers along the pillar height where image #1 is at the top of the pillar and #10 is at the bottom.

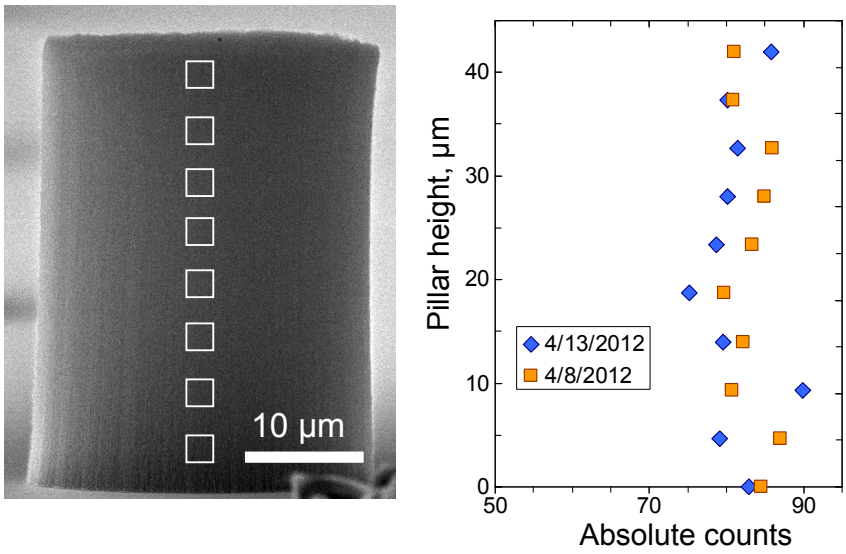

Figure S4. Results of the edge detection technique over different SEM sessions on two different days from SEM images taken along the pillar height.

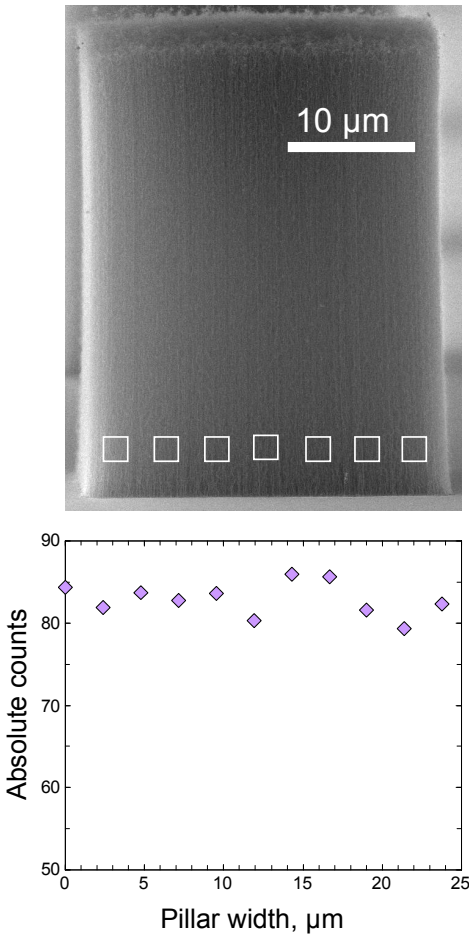

Figure S5. Variations in the absolute tube number counts across the lateral width of a pillar of square cross-section located on the edge of the Si substrate.

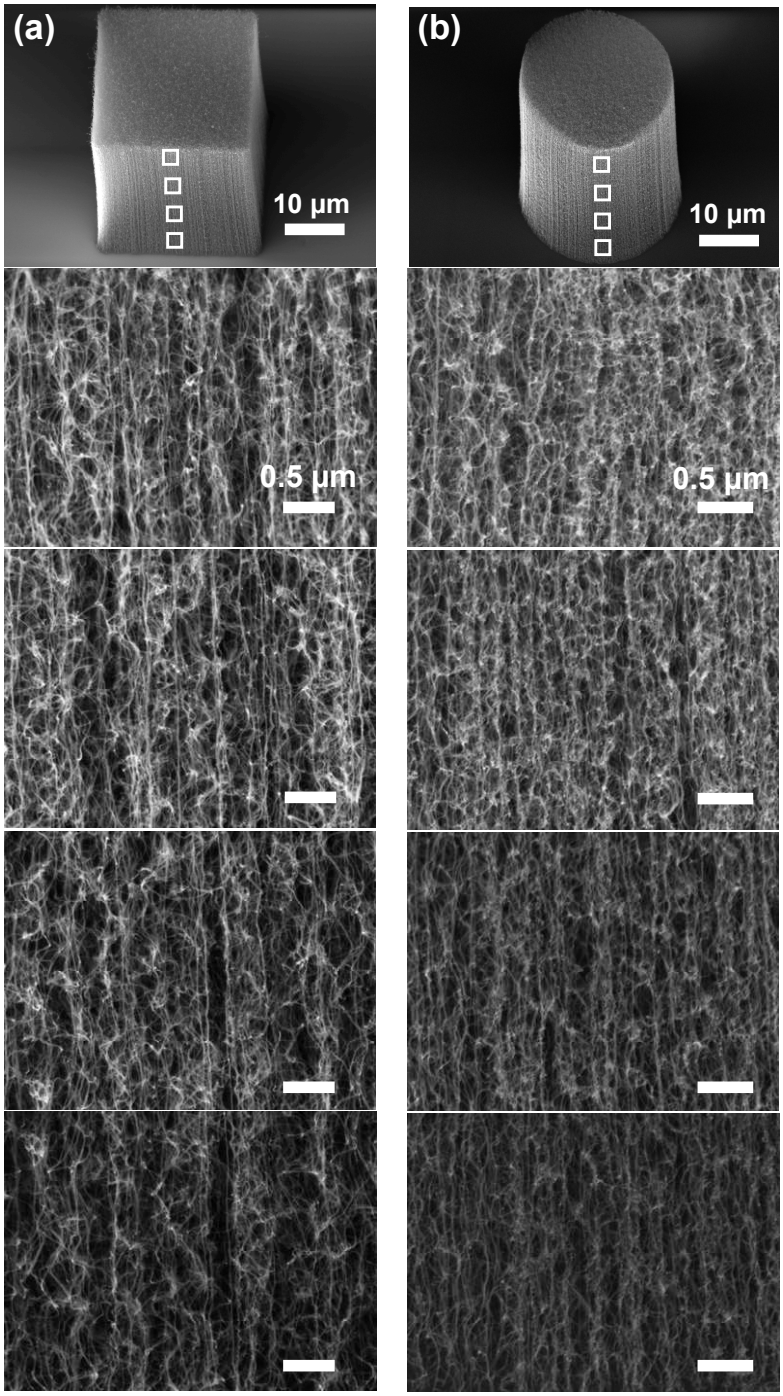

Figure S6. Representative set of four SEM images taken along the heights of the (a) pillars on the substrate-edge and (b) pillars in the interior of the substrate. The SEM images were taken at a 30 deg tilt angle.

4. Model formulation: Strength Multiplier (SM) function

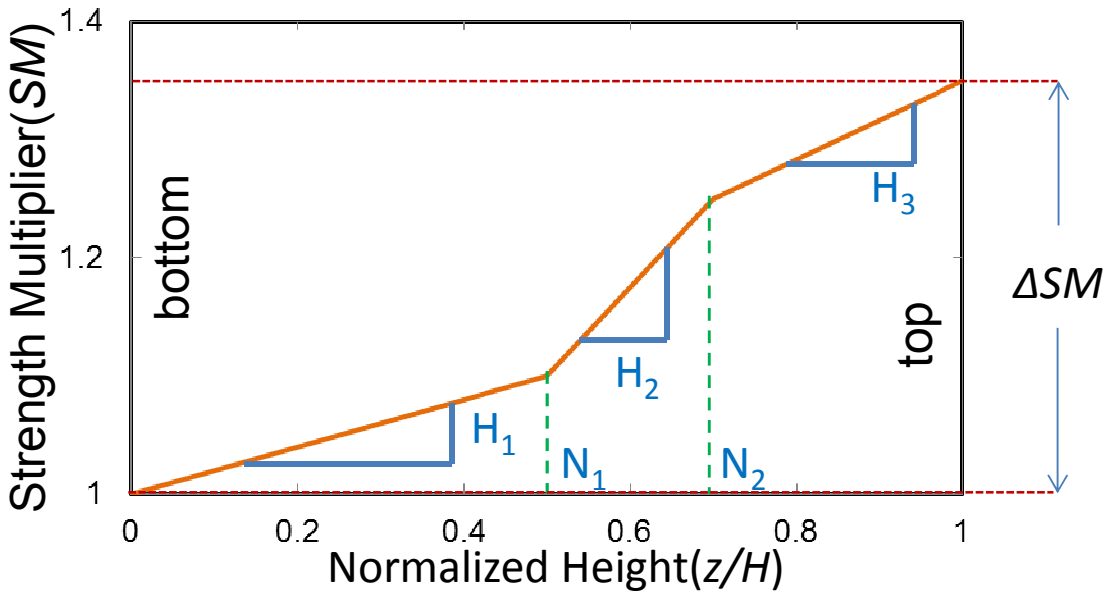

Figure S7. A three piecewise strength multiplier (*SM*) function was used along the pillar height to generate an axial gradient in property, applied on E and σ_o. The SM function can be defined using the three slopes H1, H2 and H3, the two transition strains N1 and N2 and the difference in strength between the top and bottom of the pillar, ΔSM.

5. Relationship between the location of the VACNT micro-pillar on the substrate to its deformation morphology and stress-strain response

Although two distinct pillar cross-sectional shapes (square and circular) are shown in Figs. 1 and 2, these different shapes do not appear to have any major influence on the mechanical behavior of the VACNTs (see Fig. S8). Rather the relative location of the VACNTs on the Si substrate was found to play a more key role in their resulting morphologies. This effect is demonstrated in Figs. S8 and S9 below.

In terms of their buckling behavior and the general shape of their stress-strain curves, two distinct classifications were made: "pillars on substrate edge" and "pillars in substrate interior". The pillars on the substrate edge had a bottom-to-top buckling sequence, with the top buckle forming last, and a positively sloped plateau in their stress strain curve. On the other hand the buckling sequence for the pillars in the interior of the substrate was markedly different, with the bottom buckles forming last, and the plateau region in their stress-strain curve was also nominally flat (see Fig. 2).

In terms of the location on the substrate, the "pillars on substrate edge" classification was confined to only the three rows of pillars at the extreme edge of substrate (a total of 51 pillars, three rows of 17 pillars each, Fig S9b, marked in red). Co-incidentally these pillars were square in cross-section. All the remaining pillars (including the remaining square pillars which were situated in a slightly more interior location as shown in Fig S9c, and the circular pillars shown in Fig. S9d) showed a deformation behavior characteristic of the "pillars in substrate interior" type. A total of 114 pillars showed the "pillars in substrate interior" behavior – including 34 pillars of square cross section (Fig. S9c, marked in blue) and all pillars of circular cross section (Fig. S9d, marked in green).

The square pillars on the edge of the substrate (Fig. S9b) show a sequential bottom-to-top buckling pattern as described in the manuscript (see Fig. 2 in the manuscript), where the first buckle is nucleated close to the substrate and each subsequent buckle initiates above the previous one. [5, 7] If the sample is unloaded from a maximum compression of ~70% strain, the top third of the pillar remains virtually unscathed (Fig. S9b, left panel), and the buckle closest to the pillar-top is always the last one to form (Fig. S9b, middle panel). The stress-strain signatures of these pillars show a heavily sloped plateau region.

However a different deformation signature is observed for the pillar sets on the substrate-interior (Figs. S9c and d). For these pillars the buckling no longer starts at the bottom – rather when unloaded from ~70% strain the *bottom* is completely unscathed and undeformed. For both these pillar sets, the fold at the pillar bottom (closest to the substrate) is the last buckle to form. Note also the similarity of the stress-strain response and the flatness of the plateau region between these two pillar sets shown in Figs. S9c and d, as well as their higher recovery as compared to those shown in Fig. S9b. It is worthwhile to reiterate here that both of the pillar-sets in Figs. S9c and d show a very similar response *in spite of* the obvious differences in their cross-sectional shape (square *vs.* circular).

In all the samples tested, we did not find any significant difference between the deformations of the square *vs.* circular pillars within the "pillars in substrate interior" type. The significant difference in the mechanical response was observed between the

pillars located on the substrate edge, which happened to have square cross-sections, and those in the substrate interior, which had both square and circular cross-sections.

A comparative analysis of the mechanical behavior of the pillars based on the above discussion is shown in Fig. 8. Fig. 8a shows that the unloading stiffness for pillars on substrate-interior remained virtually constant when unloaded from within the stress plateau region (E = 9.11±2.7 MPa). In contrast, the stiffness of the pillars on substrate-edge increased from $E \approx 20$ MPa to $E \approx 31$ MPa as the strain increased beyond 30%. In general, pillars on the substrate-edge appeared stiffer than the pillars on substrate interior (see Fig. S8a). The two pillar sets also differed in the amount of recovery when unloaded from post-densification regime: pillars on substrate-interior ($R \approx 57.9 \pm 0.9$ %) showed an almost 45% higher recovery than those on substrate-edge ($R \approx 39.8 \pm 3.9$ %, Fig. S8b). This shows that there was a clear distinction in the deformation and mechanical response between the samples within the distinct areas on the substrate real estate.

Figure S8c shows the comparison between the pillars of square *vs.* circular cross section as a function of location on the substrate. All pillars shown in this figure are located in the substrate-interior. As evident from this figure, there are no major differences between the pillars based on their cross-sectional shape. When located in the substrate-interior, pillars of both cross-sections show a similar range of plateau stress values (0.15 – 0.3 MPa), with the plateau stresses showing an increasing trend with faster loading rates (a behavior considered typical for viscoelastic solids)

We note that literature reports have shown buckling initiation in VACNT micro-pillars to be dictated by a combination between the local stress distribution (influenced by the shape) and the local density. [13] However as seen from Fig. S9, for this current work the shape of the pillar cross-sections can be ruled out as a potential reason for their differences in mechanical behavior and deformation morphology. Thus it is reasonable to believe here that the key distinction between the various pillar types is in their local density and its variation along the pillar height, which is apparently affected by their relative locations on the substrate. We hypothesize that the neighborhood effect, *i.e.* the effect of having another VACNT growth nearby, has a marked effect on their density during synthesis. More work is needed to determine the exact cause of these interesting effects.

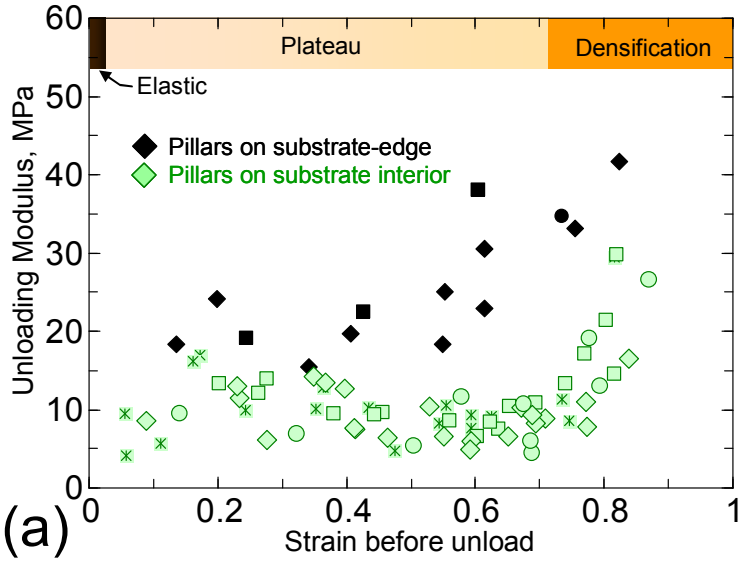

(b)	Pre-densification (plateau) regime	Post-densification regime
Pillars on substrate-edge	$R = 63.4 \pm 4.1\%$	$R = 39.8 \pm 3.9\%$
Pillars on substrate interior	$R = 65.6 \pm 1.4\%$	$R = 57.9 \pm 0.9\%$

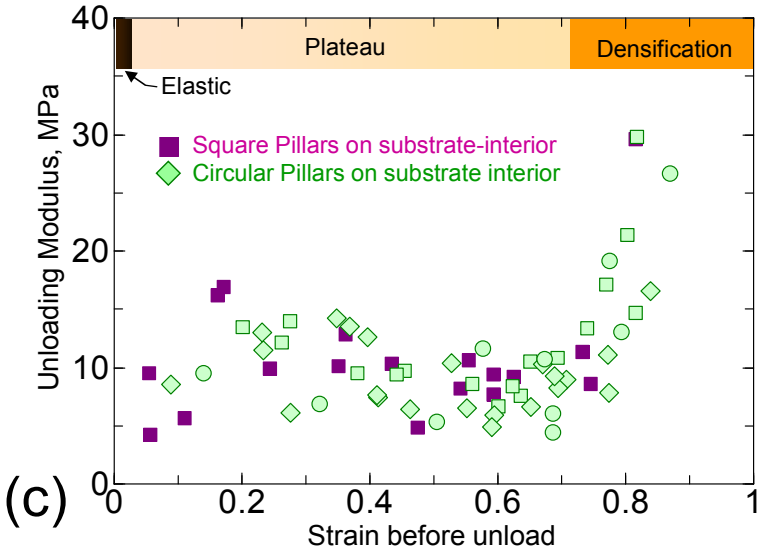

Figure S8. (a) Changes in the unloading modulus at varying maximum strains for the pillars on substrate edge *vs.* on substrate-interior showing a response similar to their respective stress-strain behavior. Tests across three loading rates 1000 nm/s (squares), 100 nm/s (diamonds) and 10nm/s (circles) are shown in this figure. (b) Table showing the % recovery (R) values in the two pillar types in their pre- and post-densification regimes.

Note that the pillars on the substrate-edge were of square cross-section, while those on substrate interior includes data for both square and circular cross-sections (see Materials and Methods)

(c) Comparison between changes in the unloading modulus for pillars of square *vs.* circular cross-sections. Note that all pillars in this figure are located in the substrate interior, and as such both sets show similar trends.

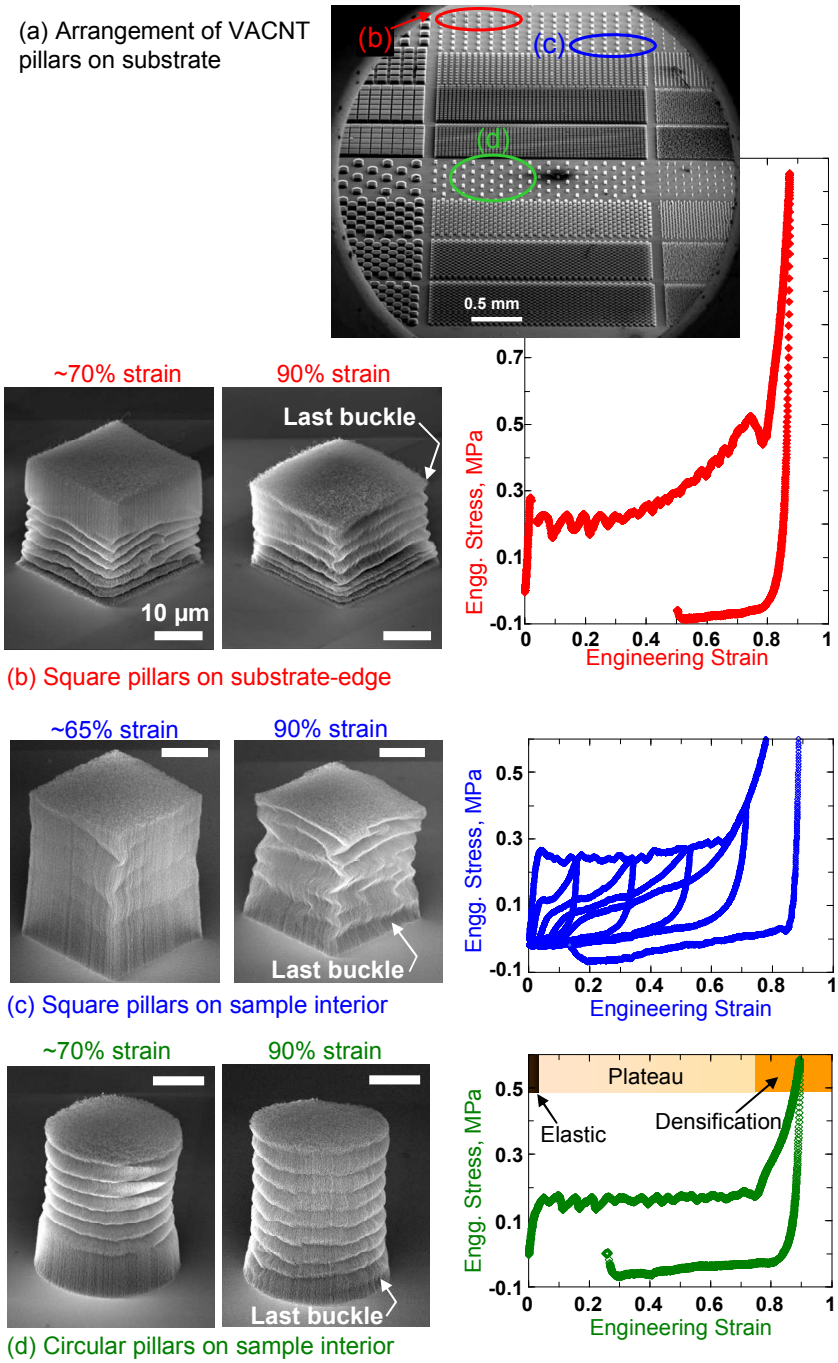

Figure S9. (a) Relative locations of the three pillar sets on the Si substrate. (b) The three rows of pillars (of square cross-section) located towards the edge of substrate show a sequential bottom-to-top buckling pattern where the top buckles are the last to form. Their stress-strain curves show a positively sloped plateau region. On the other hand all other pillar sets located on the substrate-interior, including those marked in (c) square and (d) circular pillars, showed a distinctly different buckling behavior, where the bottom buckle is the last one to form. These pillars show a flat (~zero slope) plateau

region, as well as higher recovery as compared to (a). The SEM images were taken at a 60 deg tilt angle.

1. Presser, V.; Heon, M.; Gogotsi, Y., Carbide-Derived Carbons - From Porous Networks to Nanotubes and Graphene. *Adv. Funct. Mater.* 21, 810-833.
2. McCarter, C. M.; Richards, R. F.; Mesarovic, S. D.; Richards, C. D.; Bahr, D. F.; McClain, D.; Jiao, J., Mechanical Compliance of Photolithographically Defined Vertically Aligned Carbon Nanotube Turf. *J. Mater. Sci.* 2006, 41, 7872-7878.
3. Yaglioglu, O.; Cao, A.; Hart, A. J.; Martens, R.; Slocum, A. H., Wide Range Control of Microstructure and Mechanical Properties of Carbon Nanotube Forests: A Comparison Between Fixed and Floating Catalyst CVD Techniques. *Adv. Funct. Mater.* 2012, 22, 5028-5037.
4. Kumar, M.; Ando, Y., Chemical Vapor Deposition of Carbon Nanotubes: A Review on Growth Mechanism and Mass Production. *J. Nanosci. Nanotechnol.* 2010, 10, 3739-3758.
5. Cao, A. Y.; Dickrell, P. L.; Sawyer, W. G.; Ghasemi-Nejhad, M. N.; Ajayan, P. M., Super-Compressible Foamlike Carbon Nanotube Films. *Science* 2005, 310, 1307-1310.
6. Pathak, S.; Lim, E. J.; Pour Shahid Saeed Abadi, P.; Graham, S.; Cola, B. A.; Greer, J. R., Higher Recovery and Better Energy Dissipation at Faster Strain Rates in Carbon Nanotube Bundles: An *In-Situ* Study. *ACS Nano* 2012, 6, 2189-2197.
7. Hutchens, S. B.; Hall, L. J.; Greer, J. R., *In situ* Mechanical Testing Reveals Periodic Buckle Nucleation and Propagation in Carbon Nanotube Bundles. *Adv. Funct. Mater.* 2010, 20, 2338-2346.
8. Zbib, A. A.; Mesarovic, S. D.; Lilleodden, E. T.; McClain, D.; Jiao, J.; Bahr, D. F., The Coordinated Buckling of Carbon Nanotube Turfs under Uniform Compression. *Nanotechnology* 2008, 19, 175704-1-7.
9. Zhang, Q.; Lu, Y. C.; Du, F.; Dai, L.; Baur, J.; Foster, D. C., Viscoelastic Creep of Vertically Aligned Carbon Nanotubes. *J. Phys. D Appl. Phys.* 2010, 43, 315401-1-7.
10. Cao, C.; Reiner, A.; Chung, C.; Chang, S.-H.; Kao, I.; Kukta, R. V.; Korach, C. S., Buckling Initiation and Displacement Dependence in Compression of Vertically Aligned Carbon Nanotube Arrays. *Carbon* 2011, 49, 3190-3199.
11. Yaglioglu, O. Carbon Nanotube Based Electromechanical Probes - PhD Thesis. Massachusetts Institute of Technology, 2007.
12. Canny, J., A Computational Approach to Edge Detection. *IEEE Trans. Pattern Anal. Mach. Intell.* 1986, PAMI-8, 679-98.
13. Maschmann, M. R.; Ehlert, G. J.; Park, S. J.; Mollenhauer, D.; Maruyama, B.; Hart, A. J.; Baur, J. W., Visualizing Strain Evolution and Coordinated Buckling within CNT Arrays by *In Situ* Digital Image Correlation. *Adv. Funct. Mater.* 2012, 22, 4686-4695.